17th World Conference on Earthquake Engineering, 17WCEE
Sendai, Japan - September 13th to 18th 2020

DESIGN AND PERFORMANCE OF LONG BUCKLING-RESTRAINED BRACES WITH RECTANGULAR CORES

B. Sitler[(1)], T. Takeuchi[(2)]

[(1)] *PhD candidate, Tokyo Institute of Technology, sitler.b.aa@m.titech.ac.jp*
[(2)] *Professor, Tokyo Institute of Technology, takeuchi.t.ab.m.titech.ac.jp*

Abstract

Buckling-restrained braces (BRBs) are often used in tall and large buildings. These applications tend to require exceptionally long BRBs, with 10~20m workpoint lengths (L_{wp}) and commensurate core yield lengths (L_p). However, the influence of the core and debonding interface dimensions on the compressive overstrength factor (β) and the low-cycle fatigue capacity is not yet clear for long BRBs. Previous experiments have indicated that longer BRBs exhibit greater compressive overstrength factors and lower cumulative inelastic deformations (*CID*) at fracture. This is due to friction at the higher mode buckling wavecrests between the core and restrainer assembly, which generates a highly nonuniform axial strain distribution and may have a significant effect on performance.

This paper investigates the adverse effects of the core yield length on the compressive overstrength, axial strain, and fatigue demands using finite element analysis. Simplified 2D shell models are used to parametrically analyze a range of core dimensions with yield lengths up to 14m, while detailed 3D solid models are used to examine the performance for representative long BRBs. Higher mode buckling and friction are shown to significantly amplify the compressive strain at the core ends, increasing the potential for core binding. Midspan tensile strains during the subsequent tensile cycles are also amplified due to strain ratcheting, reducing the fatigue capacity. From these results, the effect of the core dimensions and debonding interface properties on β are discussed, leading to the following findings:

1) The friction component of compressive overstrength (β_F) is confirmed to increase linearly with the friction coefficient (μ), debonding gap-to-core thickness ratio (s_w / t_c), and core slenderness (λ_F), while the associated compressive strain amplification increases the susceptibility of long BRBs to friction-induced core binding.
2) Compressive strains (ε_C) at the core ends increase linearly with the average axial strain ($\bar{\varepsilon}$) and β_F. The associated Poisson expansion may cause the core to locally bind to the restrainer in long BRBs, greatly increasing β as a function of the confining strength and stiffness of the restrainer. Therefore, a thicker strong axis debonding gap is required in long BRBs in order to prevent friction-induced core binding.
3) Tensile strains (ε_T) at mid-span during the subsequent tensile cycle increase linearly with β_F, but with the square of $\bar{\varepsilon}$. When β_F is large this may result in premature necking at midspan and is considered to be the primary cause of the reduced fatigue capacity observed in long BRBs.

Keywords: Buckling-restrained braces, Long core, Compressive overstrength, Core binding, Fatigue capacity

1. Introduction

Buckling-restrained braces (BRBs) are often used in tall and large buildings [1–3], with an early example shown in Fig. 1a. These applications tend to require exceptionally long BRBs, with 10~20m workpoint lengths (L_{wp}), and commensurate core yield lengths (L_p). To minimize welding and improve ductility, it is desirable to use a rectangular core (Fig. 1b), rather than a built-up section, such as a cruciform (Fig. 1b). However, a rectangular core will have a lower weak axis radius of gyration, shortening the higher mode buckling wavelength (Fig. 1c). This increases the number of wavecrests that develop along the core yield length, generating friction and amplifying the compressive force.

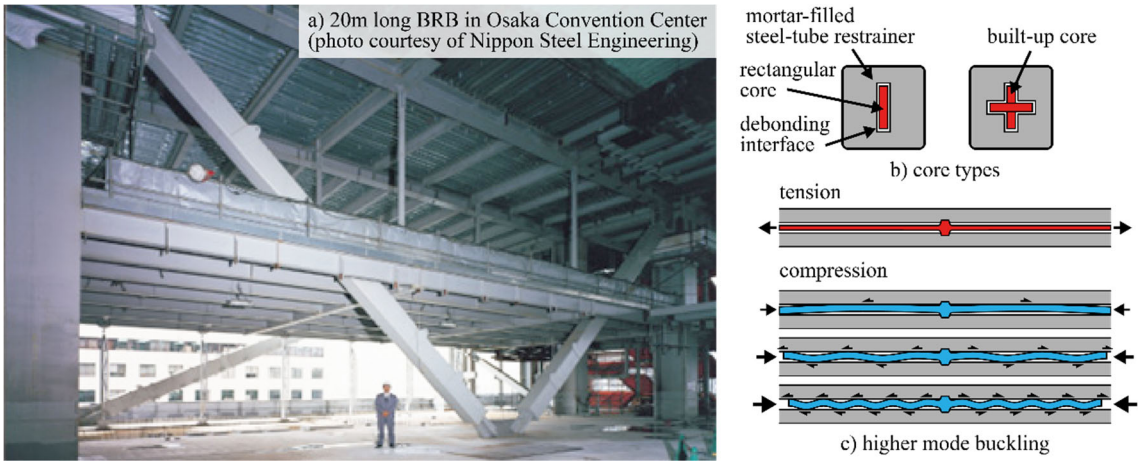

Fig. 1 – Long BRBs

Design standards [3, 4] account for this friction effect through a compressive overstrength factor (β [4]), which is defined as the ratio of peak compression (P_C) to tension (P_T) force over a symmetric test cycle (Eq. (1)). Testing is also used to confirm the fatigue capacity, which may be expressed as a cumulative inelastic deformation (*CID,* [4]) or low cycle fatigue Coffin-Manson curve [5]. However, full-scale testing is generally not required, as few facilities can accommodate specimens exceeding 10m in length.

Nevertheless, several tests [6–8] (Table 1) have compared BRBs with different core thicknesses (t_c) and yield lengths (L_p). Here, the friction contribution ($\beta_F \approx \beta / \beta_P$) is estimated by dividing β by the Poisson effect (β_P, Eq. (2)) occurring due to the applied average axial strain ($\bar{\varepsilon}$, Eq. (3)), assuming small angles and no end bearing or core binding (Section 5). Friction increases with the cumulative thrust (i.e., normal force), which depends on the higher mode buckling wavelengths (i.e., number of waves) (proportional to t_c) and debonding gap-to-wavelength ratio (proportional to the core slenderness λ_F (Eq. (4)). Therefore, the friction overstrength contribution $\beta_F - 1$ should scale with λ_F / t_c, which is confirmed by comparing the specimen pairs in Table 1.

$$\beta = \frac{P_C}{P_T} = \beta_P \beta_F \tag{1}$$

$$\beta_P = \frac{\left(1 + \nu_p \bar{\varepsilon}\right)^2}{\left(1 - \nu_p \bar{\varepsilon}\right)^2} \approx 1 + 2 \cdot \bar{\varepsilon} \tag{2}$$

$$\bar{\varepsilon} = \frac{\delta}{L_p} \tag{3}$$

$$\lambda_F = \frac{L_F}{r_c} \tag{4}$$

where δ is the applied axial displacement, $\nu_p = 0.5$ the plastic Poisson ratio, r_c the core radius of gyration ($r_c = t_c / \sqrt{12}$ for rectangular cores) and L_F the effective friction length ($L_F = L_p / 2$ with a midspan shear key).

Table 1 – Effect of core thickness and yield length

Specimen	Core	t_c (mm)	L_p (m)	λ_F	$\bar{\varepsilon}$	β	β_F	CID
WES-C [6]	SN490B, ✚	25	2.1	29	3.0%	1.11	1.05	718
WES-J [6]	SN490B, ✚	48	9.5	74	3.5%	1.16	1.08	410
			(λ_F / t_c) **×1.3**			$(\beta_F - 1)$ **×1.7**		**÷1.8**
WPSC3A [7]	A36, ━	25	3.0	205	3.5%	1.11	1.04	880
WPSC1A [7]	A36, ━	13	4.3	584	3.0%	1.31	1.23	393
			(λ_F / t_c) **×5.7**			$(\beta_F - 1)$ **×6.6**		**÷2.2**
Q10 [8]	A36, ━	32	4.5	224	3.2%	1.29	1.22	763
Q4 [8]	A36, ━	32	9.9	542	2.2%	1.65	1.58	476
			(λ_F / t_c) **×2.4**			$(\beta_F - 1)$ **×2.7**		**÷1.6**

These tests clearly indicate that β increases with long and thinner cores, resulting in significant overstrength for the slender rectangular core specimens ("━", WPSC1A and Q4). Although the reduction in *CID* is less than the increase in β, the *CID* capacity of the slender specimens approaches the expected demand during a single large earthquake [7], suggesting that a more detailed analysis may be required to justify leaving long BRBs in place through multiple events. While the built-up cruciform cores ("✚", WES-C and WES-J) exhibit similar trends, the large overstrength of the slender rectangular core specimens is the primary cause for concern, as this could lead to global instability. Therefore, a robust understanding of the interaction between friction, axial strain and β is important for the design of long BRBs, with analytical means to estimate these effects equally important when full-length testing is not available.

Simple equations to estimate β have been proposed [6, 9] based on the assumption that the compressive force is directly increased by the friction force (F) accumulated at the core wavecrests (i.e., $|P_C| = F + \beta_P P_T$), as calculated from a constant higher mode buckling amplitude and wavelength. However, these assumptions are not strictly correct, as numerical [6, 10, 11] and experimental evidence [9] indicate that the primary effect of friction is to cause forces, stress and strains to gradually decrease along the core yield length, reaching a minimum at the core-restrainer compatibility point (e.g., midspan shear key). Therefore, the increase in compressive force at the core ends results from displacement compatibility between the applied displacement and axial strains, and is not necessarily equal to F. Furthermore, this implies that the axial strains may significantly exceed $\bar{\varepsilon}$, depending on the shape of the stress-strain curve and the material's cyclic properties.

This paper numerically investigates long BRBs under a cyclic protocol. First, the influence of the core dimensions on β and the core axial strains is studied using simplified 2D models. Next, fatigue and core binding is investigated in long BRBs using calibrated 3D models. A simple empirical relationship is then proposed to estimate the compressive strain amplification from the friction component of compressive overstrength, which may be used to design the debonding gaps in long BRBs.

2. Finite element models

Simplified 2D Abaqus/Explicit models [12] were employed to parametrically investigate the effect of the core properties. Computationally expensive 3D Abaqus/Explicit solid models of a prototype BRB (Fig. 2a) were then used to investigate some of the consequences of large β values in long BRBs.

The simplified 2D models represent half of a confined rectangular core with a midspan shear key undergoing higher mode buckling about the weak axis (Fig. 2b). Each model consists of a longitudinal cross section with length $L_p / 2$ and depth t_c, with roller fixity at the far end and half the brace displacements $\pm\delta / 2$ applied at the free end. The core section is subdivided into linear reduced integration plain stress elements (CPS4R) with a mesh size of $t_c / 5 \times t_c / 5$. The restrainer is modelled with an analytical rigid surface that is offset from both the top and bottom core edges by the debonding gap thickness (s_w). The contact model features a constant friction coefficient (μ) in the tangential direction and hard overclosure in the normal direction.

A practical range of core dimensions (L_p = 2 ~ 14m, t_c = 16 ~ 40mm) and debonding gap ratios (s_w/t_c = 0.01 ~ 0.1) were selected. As there is currently insufficient experimental evidence to justify a more complex friction model, friction coefficients (μ = 0.1 ~ 0.3) were selected to bound those obtained in previous studies by matching the experimental axial forces to finite element models. Each combination of properties in Table 2 were analyzed for a total of 96 models.

The detailed 3D solid models (Fig. 2c) followed the same general modelling approach as the 2D models. The core was meshed with linear reduced integration elements (C3D8R), but using a slightly coarser subdivision (t_c / 3 × t_c / 3) to improve runtime. The midspan shear key, taper connections, steel tube and mortar infill were explicitly modelled with solid elements and a trilinear material defined at the yield (f_y, ε_y) and ultimate ordinates (f_u, ε^m_u). The 45MPa mortar was subdivided into a 10mm mesh and assigned concrete damaged plasticity properties from [13]. The core-mortar and restrainer tube-mortar interfaces were modelled with general contact, with the latter adopting a nominal friction coefficient of 0.3.

Specimen WPSC3A from [7] was adopted as the benchmark model and is referred to as W3A-3m. This specimen features a 25×148mm rectangular core, SHS 305×6.4mm mortar-filled steel-tube restrainer, L_p = 3m yield length, a midspan shear key and welded connections. Other dimensions are detailed in [7], although the A36 core was substituted with the SN400B material model calibrated in the subsequent section. The debonding gaps were taken as s_w = 1mm (s_w / t_c = 0.04) and s_s = 2mm (s_s / B_c = 0.01), and the friction coefficient as μ = 0.2, but note that these are simply representative properties, and not necessarily those of the actual specimen. Two long BRB models (W3A-10m-A and W3A-10m-B) with L_p = 10m yield lengths were then constructed. The restrainer thickness was increased to 12mm to provide a corresponding safety factor against global buckling, and a larger strong axis debonding gap provided for W3A-10m-B to accommodate greater compressive strains. The three models are summarized in Table 3.

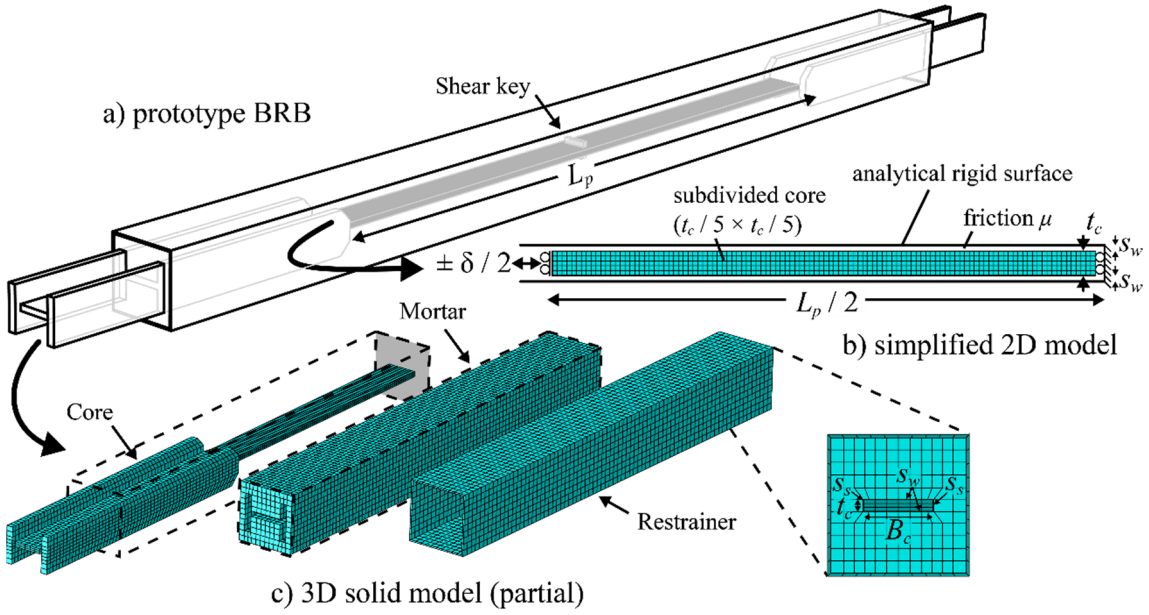

Fig. 2 – Finite element models

Table 2 - 2D model parameters

μ	t_c	s_w / t_c	L_p
-	*mm*	-	*m*
0.1	16	0.01	2
0.3	25	0.03	6
	40	0.04	10
		0.10	14

Table 3 - 3D model summary

Model	Core (t_c×B_c)	Restrainer	L_p	s_w	s_s
-	*mm*×*mm*	*mm*×*mm*	*m*	*mm*	*mm*
W3A-3m	25×148	SHS 305×6.4	3.0	1.0	1.5
W3A-10m-A	25×148	SHS 305×12	10.0	1.0	1.5
W3A-10m-B	25×148	SHS 305×12	10.0	1.0	3.0

2.1 Constitutive steel material model

SN400B was adopted for the core material. This is a common steel grade used for BRBs in Japan, and has a specified yield strength of $235 < f_y < 355$MPa, ultimate strength of $400 < f_u < 510$MPa, material overstrength of at least $f_u / f_y > 1.25$ and elongation at fracture of at least 18% [14]. In practice, the tensile overstrength (ω) at design strains is on the order of $\omega = 1.6$ [15], and while the monotonic ultimate strain ($\varepsilon^m{}_u$) generally exceeds $\varepsilon^m{}_u > 20\%$, isotropic hardening reduces the cyclic ultimate strain ($\varepsilon^c{}_u$) to about $\varepsilon^c{}_u \approx 15\%$ [16]. The cyclic coupon tests used to calibrate the constitutive material model were tested by Ono and Sato [16], and achieved $f_y^{EXP} = 259$MPa, $f_u^{EXP} = 432$MPa, $f_u^{EXP} / f_y^{EXP} = 1.67$ and $\varepsilon^m{}_u{}^{EXP} = 21\%$.

The "combined hardening" model in Abaqus is adopted [12]. This is an Armstrong-Frederic model with multiple backstresses developed by Chaboche [17], and features a cyclic yield surface (σ_0), and isotropic (Q_∞, b) and kinematic (C_i, γ_i) hardening components that develop with the true plastic strain ε^{pl}. The steady-state strain ratcheting is controlled by the near-linear third backstress (γ_3) [17] and isotropic hardening, which develops with the cumulative plastic strain (rather than previous strain range). While cyclic stresses were considered when calibrating the constitutive material model, the tangent stiffness and ultimate stress and strains are of primary importance to the higher mode buckling phenomena and compressive overstrength. The material parameters and resulting ultimate tensile stress (f_u) and strains ($\varepsilon^m{}_u$, $\varepsilon^c{}_u$) are summarized in Table 4, and an example calibrated hysteresis is depicted in Fig. 3.

Table 4 – Calibrated constitutive model parameters

Steel grade	E	σ_0	C_1	γ_1	C_2	γ_2	C_3	γ_3	Q_∞	b	f_u	$\varepsilon^m{}_u$	$\varepsilon^c{}_u$
	GPa	*MPa*	*MPa*	-	*MPa*	-	*MPa*	-	*MPa*	-	*MPa*	*%*	*%*
SN400B	205	130	52500	350	2080	13	308	1	105	5	450	24	16

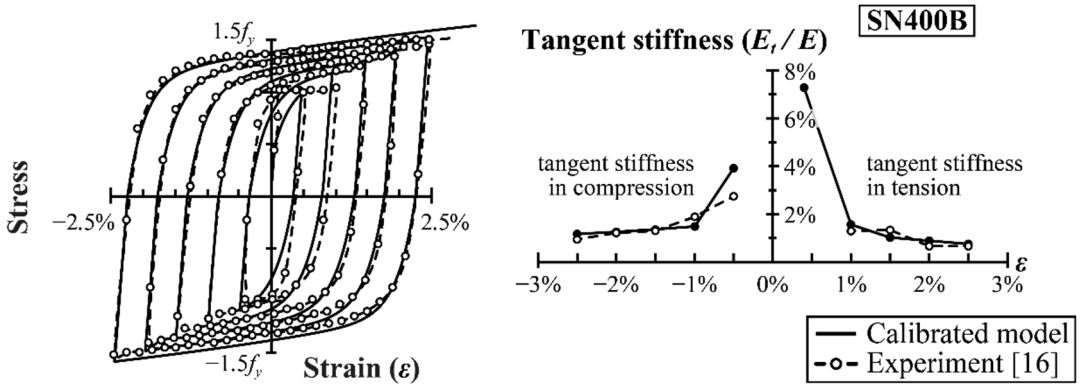

Fig. 3 – Calibrated constitutive material model (SN400B)

2.2. Displacement protocol

Two different loading protocols were adopted, with both specified in terms of the average axial strain ($\bar{\varepsilon}$) defined in Eq. 3. The 2D models were subjected to the gradually increasing, symmetric uniaxial protocol shown in Fig. 4a, which is modified from a protocol commonly used to prequalify BRBs in Japan [3] that consists of 3 cycles each at 0.5%, 1.0%, 2.0% and 3.0% strain, but split into 0.5% strain increments. Meanwhile, the 3D models were subjected to an AISC 341-16 compliant subassemblage protocol (Fig. 4b) used for the benchmark specimen [7], with equal displacements applied in the axial and transverse (in-frame) directions. The compressive overstrength was then calculated from the maximum compression (P_C) and tension (P_T) forces experienced during the second cycle at each amplitude.

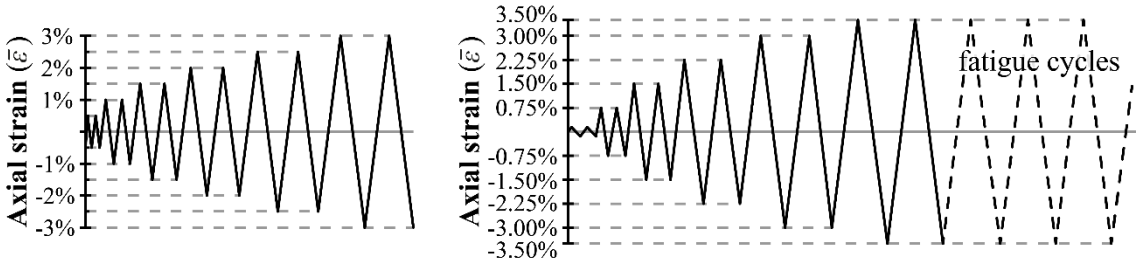

a) uniaxial protocol (2D models) b) subassemblage protocol (3D models)

Fig. 4 – Loading protocols

3. Compressive overstrength (2D model)

This section presents the results obtained from the 2D parametric study, establishing the effects of the core geometry, friction and materials on the compressive overstrength and axial strain.

3.1 Effect of core length

Increasing the core yield length accommodates more plastic higher mode buckling waves, with the lateral thrust at each wavecrest producing a small friction force. The effect of this friction force is apparent in Fig. 5a, which depicts the axial stress-strain hysteresis for four models with different core yield lengths. Higher mode buckling occurs only during the compressive cycles, as indicated by the small instabilities observed immediately after yielding in compression and which are followed by a gradual increase in the brace compressive force. Friction has no effect on the brace force during the subsequent tensile cycle.

The resulting compressive overstrength factors (β) are plotted in Fig. 5b, separated into the Poisson (β_P) and friction (β_F) contributions. While both increase with the average axial strain ($\bar{\varepsilon}$), the Poisson contribution β_P is independent of the yield length and scales linearly with $\bar{\varepsilon}$ at these relatively small strains. However, the friction contribution β_F increases in proportion to the yield length, and as a concave function of $\bar{\varepsilon}$. This is a general result for materials, such as steel, that exhibit a decreasing rate of change in stress and tangent stiffness (i.e., concave stress-strain curve). As stress and tangent stiffness in part determine the higher mode buckling wavelength, the rate of change in β_F must decrease with $\bar{\varepsilon}$, producing the concave plot in Fig. 5b.

This suggests that the β - $\bar{\varepsilon}$ plot will always be linear or concave in well-designed BRBs where the compressive overstrength is attributed solely to Poisson, higher mode buckling and stable friction effects. However, core binding, end bearing and other undesirable phenomena may cause β to increase further. For long BRBs the primary concern is core binding, where the compressive strain and resulting lateral expansion causes the core to wedge into the confining mortar, transmitting significant axial forces to the restrainer. Core binding is investigated in more detail in Section 5.

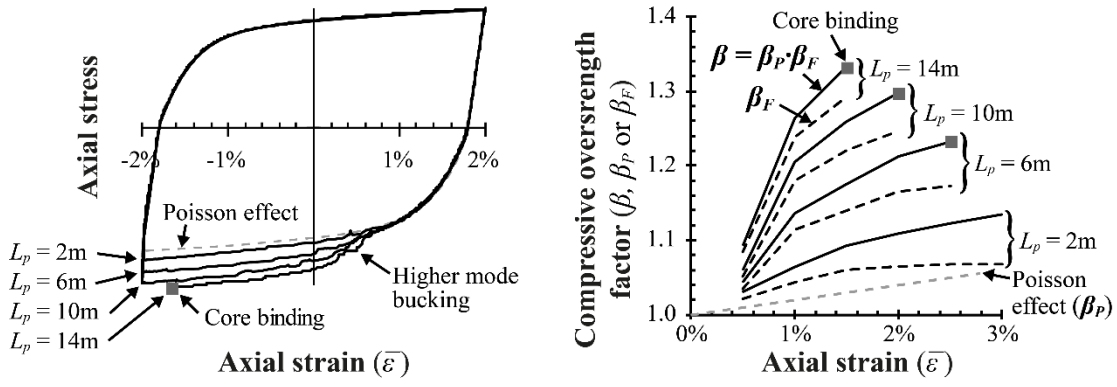

a) Core hysteresis b) Compressive overstrength

Fig. 5 – Effect of core yield length on compressive overstrength

3.2 Effect of core slenderness, debonding gap and friction

The total friction force (F) accumulated between the core ends and midspan shear key is a function of the compression force at each wavecrest, the number of higher mode buckling waves, the amplitude-to-wavelength ratio and the friction coefficient. While the compression force varies along the core [9], it may be taken as a constant without introducing a significant error for $\beta_F < 1.3$. Similarly, simply adopting the average wavelength and average amplitude offers a good approximation of the total compressive overstrength [6]. As the number of waves is proportional to λ_F, or L_p / t_c, and the wavelength-to-amplitude is proportional to s_w / t_c, the total friction force equals a strain-dependent constant multiplied by $\mu \cdot \lambda_F \cdot s_w$ / t_c.

Fig. 6 indicates that friction component of compressive overstrength (β_F) increases linearly with this indicator of total friction force. In practice, the debonding interface properties (μ, s_w) tend to be fixed for a given supplier, which suggests that the key design variables influencing β_F are limited to L_p and t_c. While the core thickness has a more pronounced effect on β_F, which for a rectangular core increases with the thickness squared, this tends to fall in a relatively narrow range of t_c = 16m ~ 40mm to avoid excessive s_w / t_c ratios or extremely thick plates. Therefore, the core slenderness λ_F is the primary concern, and for long BRBs the core yield length L_p is the main variable.

It should also be noted that β_F exhibited a near constant uncertainty of about ±0.02. While a 3% variation in force is not of engineering significance, this occurred despite the controlled numerical simulation, suggesting that it is an intrinsic uncertainty. While a detailed discussion is beyond the scope of this paper, the source of this uncertainty is the random variation in the width of individual wavecrests, which affects the number of higher mode buckling waves that develop.

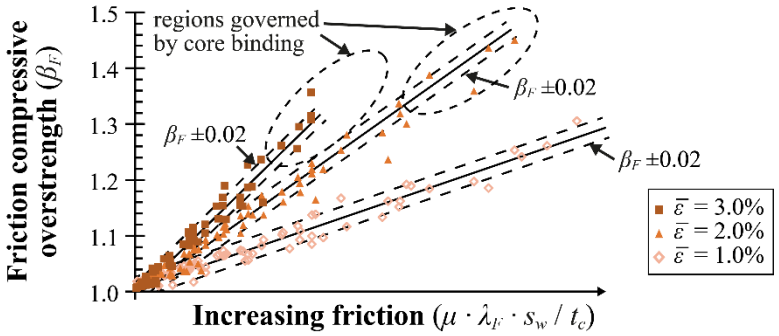

Fig. 6 – Effect of the friction coefficient, core slenderness and debonding gap on β_F

4. Axial strain amplification (2D model)

4.1 Friction and non-uniform strain distribution

Although a side effect of higher mode buckling and friction is the greater compressive forces (i.e., β_F), the direct effect is to gradually decrease the axial force along the core yield length. As the core axial force is related to the axial strain by the tangent stiffness, large changes in strain are likely to accompany modest changes in force in the plastic regime. The core end reaction is obtained by integrating the axial strains along the core and equating to the applied displacement, and then matching the strain to a stress and force. Note that this suggests that the core strain will only be $\bar{\varepsilon}$ at the quarterpoints, with larger compressive strains at the core ends and smaller compressive (or tensile) strains at midspan. This also suggests that the friction force (F) transmitted to the restrainer is about twice friction component of compressive overstrength ($\beta_F P_T$).

Furthermore, it follows that a small increase in β_F will correspond to a large increase in compressive strain (ε_C) at the core ends. However, if one assumes that the compressive engineering tangent stiffness is approximately constant, the increase in compressive strain is directly proportional to the increase in stress (and β_F). This would imply that the compressive strain amplification ($\varepsilon_C / \bar{\varepsilon}$) will decrease as the applied average axial strain $\bar{\varepsilon}$ increases, somewhat mitigating the effect.

A representative axial strain and force distribution is shown in Fig. 7. Note that bending strains due to higher mode buckling, which only occurs during compression cycles, further increase the peak compressive strains at the extreme fibres.

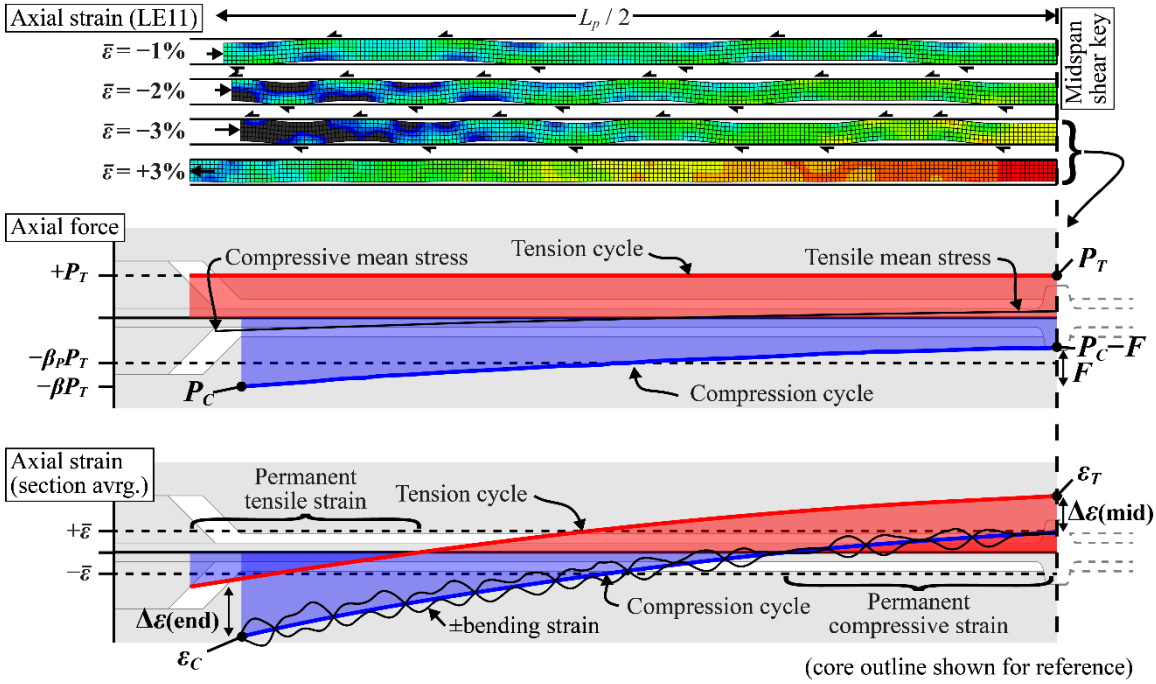

Fig. 7 – Typical axial strain distribution

4.2 Cyclic strain ratcheting

While the above description of the non-uniform axial strain and force distribution is valid for monotonic loading, the axial force at all points along the core equals P_T in the subsequent tensile cycle, suggesting that the cyclic forces are not equal in compression and tension. The core ends will cycle from $-\beta P_T$ to $+P_T$, producing a mean compressive stress, while the core midspan will cycle from $-(\beta P_T - F)$ to $+P_T$, producing a mean tensile stress.

Nonzero mean stresses are known to induce cyclic strain ratcheting [17] (Fig. 8), where strains gradually increase in the direction of the mean stress when repeatedly cycled between constant, but asymmetric stresses. As the strain ratcheting increment depends on the mean stress magnitude, strain range, and material softening / hardening characteristics, greater cyclic strain ratcheting will occur as β_F and $\bar{\varepsilon}$ increase. Therefore, while little to no ratcheting may be expected for short specimens with a negligible β_F, significant strain ratcheting may be expected in long BRBs with a large friction compressive overstrength β_F.

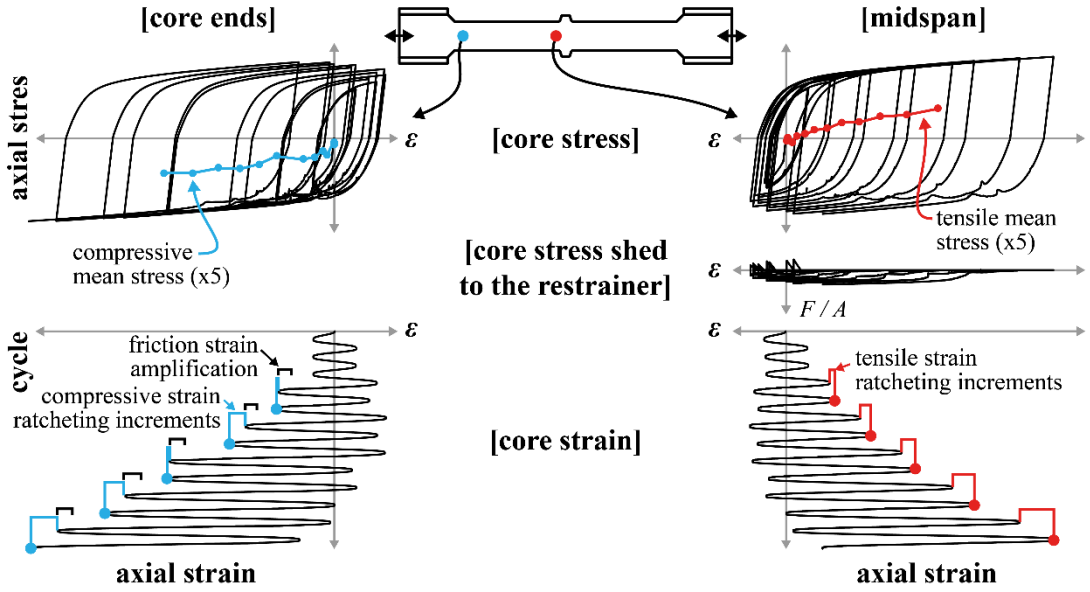

Fig. 8 – Strain ratcheting due to friction-induced mean stress

4.3 Peak axial strain amplification

The amplification of the peak compressive strains at the core ends ($\varepsilon_C / \bar{\varepsilon}$) (Fig. 9a) is due to a combination of the non-uniform compressive strain distribution produced by friction, which increases with β_F, but decreases with $\bar{\varepsilon}$, and subsequent cycle strain ratcheting, which increases with β_F and $\bar{\varepsilon}$. For the material model adopted in this study, these two effects approximately balance out, resulting in a compressive strain amplification that is solely a function of β_F, regardless of the amplitude $\bar{\varepsilon}$.

Conversely, the amplification of the peak tensile strain at the core midspan ($\varepsilon_T / \bar{\varepsilon}$) (Fig. 9b) is primarily attributed to cyclic strain ratcheting, increasing with β_F and $\bar{\varepsilon}$. The tensile strain amplification is less than the compressive strain amplification for $\bar{\varepsilon} < 3.5\%$, which covers the design range for most applications. Best-fit equations for the compressive and tensile strain amplification are listed below in Eqs. (5a) and (5b).

$$\frac{\varepsilon_C}{\bar{\varepsilon}} \approx 1 + 15\left(\beta_F - 1\right) \tag{5a}$$

$$\frac{\varepsilon_T}{\bar{\varepsilon}} \approx 1 + 15\left(0.18 - 3.1 \cdot \bar{\varepsilon} + 780 \cdot \bar{\varepsilon}^2\right)\left(\beta_F - 1\right) \tag{5b}$$

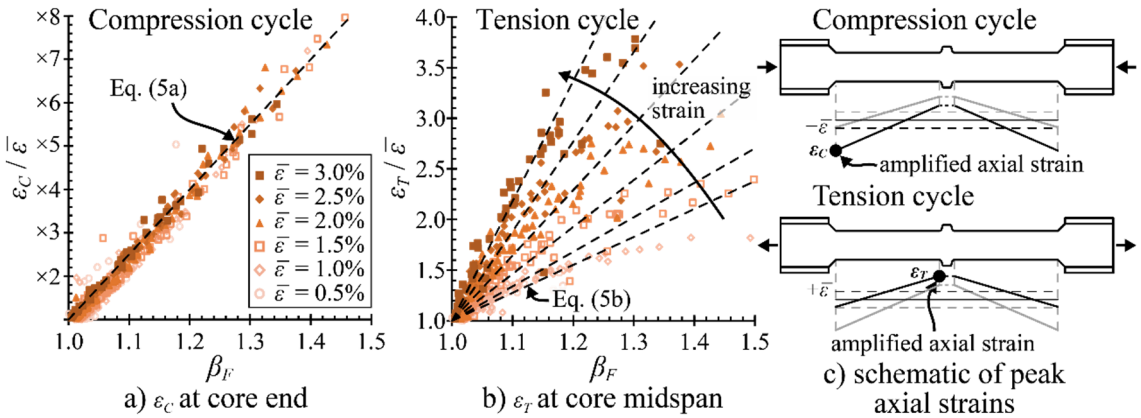

Fig. 9 – Peak axial strain amplification

4.4 Strain range amplification / reduction

Despite the potentially large peak compressive and tensile strains, these are not coincident, while cyclic strain ratcheting only gradually increases the strain amplitude. Therefore, the strain range experienced in any given cycle is far less than $\varepsilon_T + |\varepsilon_C|$. As β_F increases, the axial strain range ($\Delta\varepsilon$) at the core ends (Fig. 10a) is greater than the average strain range ($2\bar{\varepsilon}$), while the axial strain range at midspan (Fig. 10b) is less than $2\bar{\varepsilon}$, with both converging towards $2\bar{\varepsilon}$ as the amplitude increases. This suggests that the local cumulative plastic strains will not substantially differ from the average axial strain protocol, even in long BRBs. Note that this only includes the average axial strain, and the extreme fibres are also subjected to cyclic bending strains.

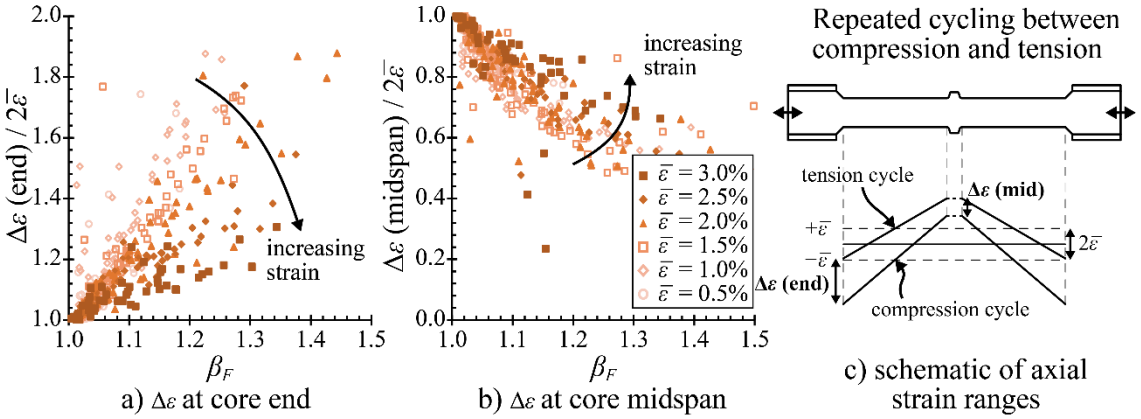

Fig. 10 – Axial strain range amplification / reduction

5. Friction-induced core binding (3D model)

The simplified 2D models indicate that β_F is accompanied by significant compressive strain amplification at the core ends. This introduces a risk of localized friction-induced core binding, where the lateral expansion of the core exceeds the debonding gap, wedging the core into the restrainer and rapidly increasing β. The critical strain at which core binding starts to occur may be conservatively estimated from the weak (s_w / t_c) and strong axis (s_s / B_c) debonding gap ratios, with the strong axis ratio almost always governing. Mortar deformation and damage increase the effective gaps (s_w and s_s), and so the critical binding strain (ε_{bind}) will slightly exceed Eq. (6), which is calculated taking the plastic Poisson ratio as $\nu_p = 0.5$, and s_w and s_s as the as-built thicknesses of the debonding layers, per face. Nevertheless, this is a conservative first estimate.

$$\varepsilon_{bind} = \min\left\{\frac{2s_w}{0.5t_c}, \frac{2s_s}{0.5B_c}\right\} \tag{6}$$

Detailed 3D models (Fig. 2c, Table 3) were analyzed to study this phenomenon. Note that W3A-3m and W3A-10m-A (s_s / B_c = 0.01) feature critical binding strains ($\varepsilon_{bind} \approx 4.0\%$) that only slightly exceed the average axial strain demand ($\bar{\varepsilon}$ = 3.5%), while W3A-10m-B (s_s / B_c = 0.02) has a larger strong axis debonding gap and a critical binding strain of $\varepsilon_{bind} \approx 8\%$. As W3A-3m experienced $\beta^{EXP} = 1.07$ ($\beta_F{}^{EXP} \approx 1.03$) at $\bar{\varepsilon}$ = 2.25% during testing, the extrapolated compressive strains $\varepsilon_C \approx 5.4\%$ ($\varepsilon_C / \bar{\varepsilon} \approx 1+15(\beta_F - 1) = 2.4$ and $\beta_F \approx (\beta_F{}^{EXP} - 1) \cdot L_{wp}/L_{wp}{}^{EXP} = 1.09$) suggest that W3A-10-A will start to experience core binding at $\bar{\varepsilon}$ = 2.25%. Note that ε_C refers to the cross-sectional average of the logarithmic axial strain (LE11).

5.1 Friction-induced core binding

The finite element results are shown in Fig. 11. The benchmark model (W3A-3m) experienced $\beta = 1.07$ at $\bar{\varepsilon}$ = 2.25% and 1.12 at $\bar{\varepsilon}$ = 3.5% (final cycle) (Fig. 11b), in good agreement with the experimental values of $\beta^{EXP} = 1.07$ and 1.11. However, the minimal friction contributions ($\beta_F = 1.02 \sim 1.04$) suggest that the numerical and experimental results were likely influenced by the expected uncertainty of β_F ±0.02. Although the core strains were not directly measured in the experiment, the finite element model indicated peak

compressive strains of ε_C = 4.4% ~ 5.6% at the critical section through 7 cycles at $\bar{\varepsilon}$ = 3.5%, which agree with the prediction of Eq. (5a) ($\varepsilon_C \approx$ 5.3%) and only slightly exceed the critical binding strain (ε_{bind} = 4.0%).

The longer model (W3A-10m-A) experienced β = 1.16 at $\bar{\varepsilon}$ = 2.25% (Fig. 11b), with the compressive strains just exceeding ε_{bind}. Noticeable core binding occurred during the next cycle (Fig. 11c), eventually developing a compressive overstrength of β = 1.41 at $\bar{\varepsilon}$ = 3.5%. This 26% increase in compressive force relative to W3A-3m is of engineering significance and would likely cause global out-of-plane buckling if not accounted for in design. Note that this model was not intended to assess stability, which depends on many other design aspects (e.g., connections, adjacent framing and global imperfections) that may be set independently.

The final model (W3A-10m-B) features a larger strong axis debonding gap (s_s / B_c = 0.02) to accommodate greater compressive strain amplification. As a result, the compressive overstrength increased in proportion to the core yield length, with β = 1.14 at $\bar{\varepsilon}$ = 2.25% and β = 1.23 at $\bar{\varepsilon}$ = 3.5%. The compressive strains at the critical section reached ε_C = 8.0%~10.6% through 4 cycles at $\bar{\varepsilon}$ =3.5%, the last two of which the midspan tensile strain exceeded the ultimate strain (ε_u^c = 16%), resulting in concentrated necking and early fracture.

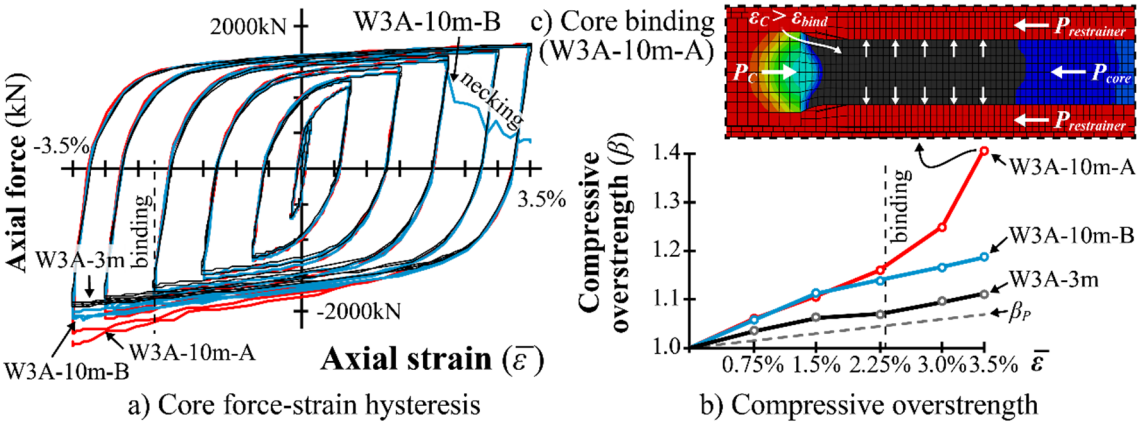

a) Core force-strain hysteresis b) Compressive overstrength

Fig. 11 – Finite element results and friction-induced core binding

By preventing core binding, W3A-10m-B retained a concave β - $\bar{\varepsilon}$ plot (Fig. 11b) with predictable and stable compressive forces. Conversely, increasing the core length for W3A-10m-A without checking the strong axis debonding gap resulted in poor performance, with core binding causing an abrupt increase in compressive force. Furthermore, the post-binding compressive force is proportional to the confining stiffness and strength of the restrainer, which depends on the mortar age and restrainer shape (e.g., SHS to CHS). However, this is not to suggest that weaker concrete or SHS restrainers should be preferred, as confining strength is beneficial in preventing bulging, another key limit state. The potential for core binding implies that short specimens may not reliably predict β for longer BRBs and tests exhibiting a sudden, accelerating trend in β (excluding minor deviations that revert to a smooth, concave β - $\bar{\varepsilon}$ plot at larger amplitudes) should be treated with caution, as the compressive force of the as-built BRB may be underestimated.

5.2 Design procedure to prevent friction-induced core binding

Therefore, a practical approach to designing long BRBs is proposed as follows:

Step 1) Retain the same weak axis debonding gap, and extrapolate β_F from previous tests (scale $\beta_F - 1$ by the change in $\mu \cdot \lambda_F \cdot s_w / t_c$) or estimate analytically [6, 9, 10], accounting for a potential uncertainty of $\beta_F \pm 0.02$.

Step 2) Calculate the peak compressive strain ε_C from the scaled β_F, design strain $\bar{\varepsilon}$ and amplification ε_C / $\bar{\varepsilon}$ indicated by Eq. (5a). This will likely indicate large compressive strains on the order of 5 ~ 20%.

Step 3) Design the strong axis debonding gap (s_s) and check that the peak compressive strain ε_C equals or exceeds the critical binding strain ε_{bind} (Eq. (6)). Do not specify an excessive strong axis debonding gap.

Step 4) Recheck strong axis bulging (e.g., [3]) or test a shorter specimen with the thicker strong axis debonding gap, particularly if a rectangular core and SHS restrainer is employed.

6. Conclusions

The effects of higher mode buckling and friction in long, rectangular core BRBs were investigated using simplified 2D and detailed 3D solid models. Compressive overstrength was found to be accompanied by significant axial strain amplification, which may result in undesirable performance in long BRBs.

1) Friction compressive overstrength (β_F) was found to increase linearly with the friction coefficient (μ), debonding gap-to-core thickness ratio (s_w / t_c) and core slenderness (λ_F), in the absence of core binding.
2) Compressive strains (ε_C) at the core ends increase linearly with the average axial strain ($\bar{\varepsilon}$) and β_F. The associated Poisson expansion may cause the core to locally bind to the restrainer in long BRBs, rapidly increasing β, with post-binding forces depending on the confining strength and stiffness of the restrainer.
3) Simple empirical equations are provided to estimate the compressive strain amplification and the strong axis debonding gap thickness required to prevent friction-induced core binding in long BRBs.
4) Tensile strains (ε_T) at mid-span during the subsequent tensile cycle increase linearly with β_F, but with the square of $\bar{\varepsilon}$ due to cyclic strain ratcheting. When β_F is large this may result in premature necking at midspan, helping to explain why long BRBs would have lower fatigue capacities.

In summary, the effects of β on the peak compressive and tensile strains must be carefully considered when designing long BRBs, particularly when full scale testing is not possible.

References

[1] Joseph L, Gulec K, Schwaiger J (2016): Wilshire Grand: Outrigger designs and details for a highly seismic site. *International Journal of High-Rise Buildings*, **5** (1), 1–12.

[2] Almufti I, Krolicki J, Crowther A (2016): The resilience-based design of the 181 Fremont Tower. *Structure Mag.*

[3] Takeuchi T, Wada A (2017): *Buckling-restrained braces and applications*. Japan Society of Seismic Isolation.

[4] AISC (2016): *Seismic provisions for structural steel buildings, AISC/SEI 341-16*.

[5] Yoshikawa H, Nishimoto K, Konishi H, Watanabe A (2010): Fatigue properties of unbonded braces and u-shaped steel dampers. *Nippon Steel Technical Report*, **1**, 84-91. (in Japanese)

[6] Tsai KC, et al. (2014): Welded end-slot connections and debonding layers for buckling-restrained braces. *Earthquake Engineering and Structural Dynamics,* **43**, 1785–1807.

[7] Terashima M (2018): *Ductile fracture simulation and risk quantification of buckling-restrained braces under earthquakes*. PhD Dissertation, Stanford University.

[8] Richards PW, Saxey B (2017): Quantifying length-effects on buckling-restrained braces that are considerably longer than the associated qualification tests. *2017 NZSEE Conference*, Wellington, New Zealand.

[9] Midorikawa M, et al. (2014): Buckling-mode number and compressive-to-tensile strength ratio of buckling-restrained braces. *10th US National Conference on Earthquake Engineering*, Los Angeles, United States.

[10] Dehghani M, Tremblay R (2017): An analytical model for estimating restrainer design forces in bolted buckling-restrained braces. *Journal of Constructional Steel Research*, **138,** 608–620.

[11] Budaházy V, Dunai L (2015): Numerical analysis of concrete filled buckling restrained braces. *Journal of Constructional Steel Research*, **115**, 92–105.

[12] Smith M (2017): *ABAQUS/Explicit User's Manual, Version 2017*. Dassault Systèmes Simulia Corp.

[13] Nguyen NH, Whittaker AS (2017): Numerical modelling of steel-plate concrete composite shear walls. E*ngineering Structures*, **150**, 1–11.

[14] JIS (2012): *Rolled steels for building structures, JIS G 3136*. Japanese Industrial Standards. (in Japanese)

[15] AIJ (2014): *Recommended provisions for seismic damping systems applied to steel structures, Chapter 3: Buckling-restrained braces*. Architectural Institute of Japan. (in Japanese)

[16] Ono T, Sato A (2000): Modeling of stress-strain relationships of metallic materials. *Journal of Structural and Construction Engineering (Transactions of AIJ)*, **65** (532), 177–184. (in Japanese)

[17] Lemaitre J, Chaboche JL (1992): *Mechanics of solid materials*. Cambridge University Press.

